Efficient Solventless Dehydrogenation of Formic Acid by a CNC-Based Rhodium Catalyst

Pablo Hermosilla,[a] Asier Urriolabeitia,[b] Manuel Iglesias,[a] Víctor Polo,[b] and Miguel A. Casado[a,*]

Complex [(CNC)^{Mes}Rh(PMe$_2$Ph)]PF$_6$ (**1**) has been found to be an effective catalyst for solventless formic acid (FA) dehydrogenation, affording exclusively H_2 and CO_2 as decomposition products. The effect of the addition of a base as co-catalysts was studied, finding that HCOONa was the most efficient additive in terms of catalyst efficiency with a catalyst loading of 0.016 % mol, reaching TOF$_{max}$ values up to 5869 h^{-1}. Additionally, we observed that adddition of water dramatically increased the catalytic activity in FA dehydrogenation, obtaining TOF$_{max}$ values up to 10150 h^{-1}. Additionally, VT kinetic NMR experiments allowed us to estimate the activation energy ($\Delta G^{\ddagger}$ = 18.12 ± 1.17 kcal mol^{-1}) of the FA dehydrogenation catalysed by **1**. Stoichiometric NMR experiments, aimed to shed light on the nature of possible catalytic intermediates, allowed us to detect and further isolate the Rh^{III} hydrido formate complex [(CNC)^{Mes}Rh(κ^O-OC(O)H)(PMe$_2$Ph)H]PF$_6$ (**2**), which originates from an oxidative addition of FA to **1**; additionally, we could detect a bis(hydrido) Rh^{III} complex [(CNC)^{Mes}Rh(PMe$_2$Ph)H$_2$]PF$_6$ (**1-H$_2$**), which is another operative intermediate in the catalytic FA dehydrogenation by **1**. DFT calculations performed on the catalytic FA dehydrogenation perfectly accounted for the gathered experimental data; the approach of a FA molecule to **1** leads to the O–H oxidative addition producing κ^O-formate intermediate **2**, which subsequently undergoes a FA-assisted isomerization to the κ^H-formate species. Further hydride abstraction generates the dihydrido intermediate **1-H$_2$**, which releases H_2 upon interaction with another FA molecule closing the catalytic cycle. The rate-limiting step in the catalytic process corresponds to the hydride abstraction step, which agrees with the KIE values estimated by NMR experiments.

Introduction

The use of hydrogen as an energy vector has received increasing interest in recent years, mainly due to the need for an urgent transition from a fossil fuel-based energy system to more sustainable alternatives. The energy surplus generated by renewable sources during low-demand periods can be stored as hydrogen by water electrolysis, which is considered a viable solution to the problems related to their intermittent nature.[1] However, the low volumetric energy density of H_2 rises concerns over its storage and transportation. On these grounds, the use of hydrogen carriers has been proposed as a means to circumvent the storage and safety issues associated with H_2. Among the hydrogen carriers proposed in the literature, formic acid (FA) offers great promise due to the fact that its gravimetric and volumetric energy densities are higher than those of compressed hydrogen, it presents low toxicity and flammability, it is environmentally benign and a liquid under atmospheric conditions.[2] Moreover, FA can be obtained from renewable sources; namely, CO_2 hydrogenation,[3] biomass oxidation,[4] and as a by-product of the synthesis of acetic acid.[5]

Formic acid dehydrogenation (FADH) has been extensively studied in the presence of solvents and in the FA/Et$_3$N azeotropic mixture, with Ir and Ru homogeneous catalysts being the most successful.[6] However, in these cases, the gravimetric and volumetric energy densities of the reaction mixtures are intrinsically lower than those of pure FA and, consequently, solvent-free conditions are desirable for FADH. To date, only Ir[7] and Ru[8] catalysts for solvent-free FADH have been reported. Catalysts **A** and **B** reported by Gelman (TOF = 11760 h^{-1}) and Fischmeister (TOF = 5122 h^{-1}), respectively, contain participative ligands able to interact with FA via hydrogen bond interactions. On the other hand, Ir complexes **C** and **D** described by Williams (TOF = 13320 h^{-1}) and us (TOF = 11590 h^{-1}), respectively, and the Ru complex (**E**) recently reported by Milstein (TOF = 3067 h^{-1} without additives or solvent, TON over 1.7 million) are able to efficiently carry out the dehydrogenation of FA without the participation of ancillary ligands (Fig. 1).

Regardless of whether the ligand plays an active or a passive role in the reaction mechanism, its design is key to tune the activity of the catalyst. In the case of non-participative ligands, although less conspicuous, their architecture defines the stability and activity of the catalyst. A common feature in complexes A-E is the presence of pincer, or chelate ligands that confer stability to the system, while providing electron density to the metal center by means of strongly donating wingtip groups—e.g., phosphanes, a tertiary alkyl in **A**, an *N*-heterocyclic olefin in D, or an amido moiety in E—or co-ligands, namely, a Cp* ligand in **B**.

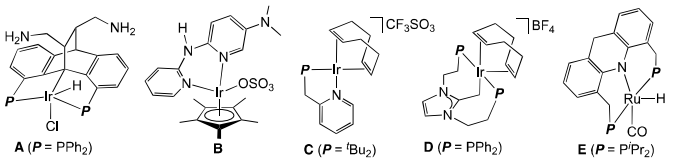

Fig 1 Selected examples of catalysts for FA dehydrogenation.

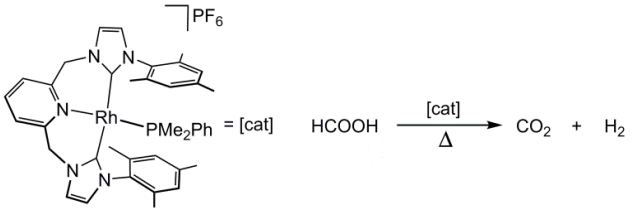

Scheme 1 Complex $[(CNC)^{Mes}Rh(PMe_2Ph)]PF_6$ (**1**) as catalyst in FA dehydrogenation.

The presence of an electron-rich metal center facilities the oxidative addition of FA's O–H bond, while rendering more nucleophilic hydrides, which consequently undergo protonation to generate H_2 straightforwardly.

On these grounds, we set off to study the impact on the catalytic activity of pincer ligands featuring strongly donating *N*-heterocyclic carbenes (NHCs) as wingtip groups.[9] More specifically, we were interested in the chemistry of a pincer ligand based on a lutidine core bearing two NHCs moieties in combination with rhodium, namely complex $[(CNC)^{Mes}Rh(PMe_2Ph)]PF_6$ (**1**) (Scheme 1).[10] Herein we report the catalytic activity of complex **1** in FA dehydrogenation under solvent-free conditions at 353 K to yield exclusively carbon dioxide and dihydrogen. The catalytic efficiency can be tuned by addition of sodium formate and also by the presence of water. DFT calculations in combination with NMR techniques provided valuable insights into the operative FA dehydrogenation mechanism.

Results and discussion

Complex **1** was evaluated as catalyst for the dehydrogenation of FA under base-free conditions in acetonitrile. However, we did not observe any transformation when FA (0.53 mmol) was dissolved in acetonitrile (1 mL) at 353 K for 1 h in the presence of 1 (1 mol %). Then we studied the effect of a base in order to assess whether **1** could act as catalyst in FA dehydrogenation;[11] in this line, addition of bases such as triethylamine, KHDMS or Na_2CO_3 under similar conditions did not alter the results in a remarkable way. However, upon addition of HCOONa (10 mol %), catalyst 1 decomposed FA (20 µL, 0.53 mmol) at 353 K in less than one minute, resulting in the production of a gaseous mixture. It is worth mentioning that the related complexes $[(CNC)^{Mes}Rh(L)]PF_6$ (L = CO, $NCCH_3$),[10] bearing non-phosphine ligands, did not show any catalytic activity on FA dehydrogenation under the same conditions.

Due to these encouraging preliminary results in catalytic FA dehydrogenation in acetonitrile, we aimed at exploring the activity of complex **1** on FA dehydrogenation under solventless conditions. For that reason, we carried out some catalytic runs with variable amounts of HCOONa as co-catalyst (Table 1). In this context, the use of a base is a common feature in many catalytic systems in FA dehydrogenation, because it may play a role as a buffer solution to control the pH of the medium and also it may be able to cleave FA dimers formed by hydrogen bonds in solution.[12] In this regard, a number of reports have proved that the activity of the catalyst strongly depends on the pH of the solution, with optimum values usually observed between pH =3–4.[13,14] Moreover, recent reports show that variable amounts of HCOONa and water in the catalytic system may help to improve the catalyst activity in both homogeneous[15] and heterogeneous approaches.[16]

Table 1 Catalytic dehydrogenation of FA by **1** in the presence of variable amounts of HCOONa.

Entry	mol % HCOONa	TON	TOF_{max} (h^{-1})
1	5	150	849
2	10	235	3329
3	20	586	5182
4	30	2014	4634
5	40	3195	5869

[a] General conditions: FA (2 mL, 53.01 mmol), complex **1** (7.5 mg, 0.016 mol %) and the specified amount of HCOONa, at 353 K.

Catalyst **1** is air stable, although the activities in FA dehydrogenation are lower if the catalytic experiments are carried out under air. Therefore, the catalytic experiments are best performed in a high-pressure reaction vessel, which was charged with the rhodium catalyst **1** (0.016 %) and sodium formate under an argon atmosphere. Complex 1 decomposed FA (2 mL, 53.01 mmol) with HCOONa as co-catalyst (5-40 mol %) at 353 K (Table 1). A catalytic run resulted in the production of 27.1 mmol of H_2 (51% conversion, TON 3195) after 1h with 40 mol % of HCOONa (Table 1, Entry 5).

When 1 was dissolved in a mixture FA/HCOONa, the initial red solution turned to yellow. When the reaction was finished, a yellow solution remained in the flask when low base loadings were used (5-10 mol %); however, when HCOONa concentrations exceeded 10 mol %, solid HCOONa remained at the bottom of the reactor at the end of the reaction. When HCOONa reaches 20 mol %, the solution becomes saturated and a yellow suspension was formed during FA dehydrogenation, which may lead to diffusion problems throughout the reaction. Although TON values are not very high (TON = 3195), when the amount of HCOONa is between 5-40 mol %, TOF values show excellent catalytic activities, reaching a TOF of 5869 h^{-1} operating at 40 mol % of HCOONa (Fig 2; Table 1, entry 5).

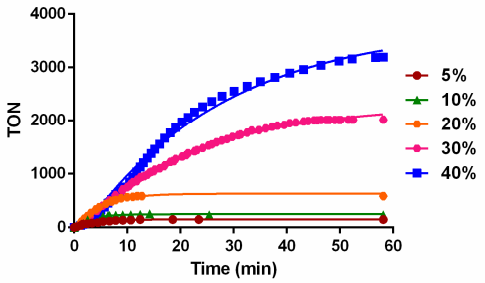

Fig. 2 Reaction profiles of FA dehydrogenation of neat FA by **1** under different HCOONa concentrations at 353 K.

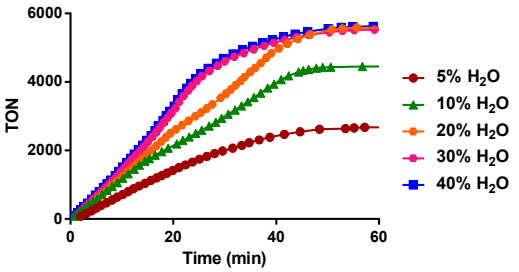

Fig. 3 Reaction profiles of FA dehydrogenation of neat FA by **1** under different H_2O concentrations at 353 K.

The overall catalytic activity increases with co-catalyst concentrations higher than 20 mol %. As Fig. 2 shows, the rate of hydrogen production is linear at the beginning of the reactions, and their slope increases with higher HCOONa concentrations, reaching its maximum close to 20 min when 40 mol % of HCOONa is used. After this point, the activity of the catalyst decreases with time. Additionally, we studied the dependence of the catalytic activity on the H_2O concentration in the catalytic media. These experiments showed that, not only the catalyst is stable under a wet environment, but also the presence of water increases the catalytic efficiency (See Figure S3). In this way, addition of increasing amounts of water into the catalytic reactions (5 to 40 mol % H_2O) enhanced the catalytic activity (Fig. 3). From 5 to 10 mol % of water a fast increase of the catalytic activity was observed, which becomes slower upon reaching a maximum TOF value at 40 mol % of water.

Table 2 and Fig. 3 show the TON values obtained at different water loadings. In particular, a catalytic run produced 47.7 mmol of H_2 (94 % conversion) with a TON number of 5625, and reaching an excellent TOF value[§] of 10150 h^{-1} (Table 2, entry 5). This is the highest TOF value reported for a Rh-based catalyst up to date[17] and compares well with the most active catalysts hitherto reported for the solventless dehydrogenation of FA (**A**-**D**).[7,8]

Table 2 Catalytic activity dependence on the addition of variable mol % of H_2O in FA dehydrogenation by **1**.

Entry	Mol % H_2O	TON	TOF_{max} (h^{-1})
1	5	2673	4319
2	10	4454	7034
3	20	5589	7740
4	30	5525	9784
5	40	5625	10150

[a] General conditions: 0.016 mol % of **1**, 30 mol % HCOONa and FA (2 mL, 53.01 mmol), and the specified amount of H_2O at 353 K.

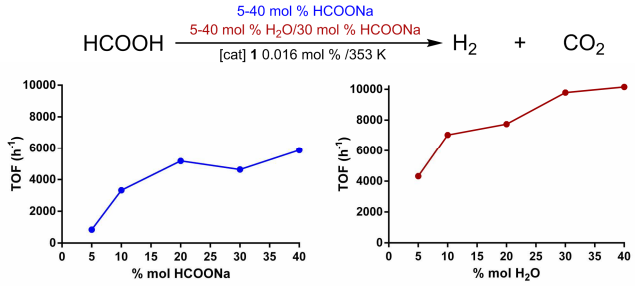

Fig. 4 TOF_{max} values variation in function of mol % HCOONa (left, blue line) and mol % H_2O (right, red line).

The enhancement of the catalytic efficiency induced by water can be understood from different perspectives; on one hand, it may favor dissociation of FA dimers and increase co-catalyst solubility; in this line, it is known that FA molecules arrange as dimers via hydrogen bonds, where the presence of water may help to dissociate such dimers leading to an easier accessibility of FA molecules to the catalytic species, therefore increasing the catalytic activity.[12] On the other hand, H_2O molecules may play an active role in the stabilization of catalytic intermediates, act as proton shuttles or even participate in hydrogen bonding with FA.[18] Fig. 4 shows comparative graphs of the dependence of the catalytic activity of **1** (0.016 mol %) with HCOONa and water, respectively. The graphic on the left shows the variation of the catalytic activity of **1** with variable amounts of HCOONa without water, while the graphic on the right shows its variation under 30 mol % of HCOONa with variable amounts of water. Note that although a 20 mol % loading of HCOONa leads to a higher initial TOF than at 30 mol %, the TON values are significantly higher in the case of the latter (Fig. 2), which prompted us to optimize the H_2O loading employing 30 mol % HCOONa. The variation of both parameters has similar effects in the catalyst activity, as shown in Fig. 4.

It is important to stress that decreasing the catalyst **1** loading to 0.005 mol % (2.16 mg, 2.6 μmol) led to a remarkable increase of the TOF value up to 11164 h^{-1} when working with 30 mol % of HCOONa and 30 mol % of water at 353 K. However, this high TOF value is encompassed with a reduction in the TON number (850). A rather important aspect associated with catalytic FA dehydrogenation is that it is desirable that FA decomposition be selective toward H_2 and CO_2 production, therefore avoiding the formation of carbon monoxide, which has been reported to damage fuel cells.[1c] In order to assess this issue, the gaseous mixture obtained under optimized conditions (neat FA, 40 mol % HCOONa, 0.016 mol % of **1**) was subjected to analysis by IR spectroscopy and GC-MS analysis, showing no traces of CO. Therefore, under our experimental conditions, the CO gas produced in the catalysis is below the detection limit (Fig. S5-S6).

We also studied the effect of temperature in the catalytic performance of **1** on FA dehydrogenation; as Fig 5 shows, increasing the temperature leads to enhanced reaction rates. The activation energy ($\Delta G^{\ddagger}$) for the solventless FA dehydrogenation catalyzed by complex **1** was estimated experimentally between 333-353 K by the Eyring/ plot ($\Delta G^{\ddagger}$ = 18.12 ± 1.17 kcal mol^{-1}; Figure S26).

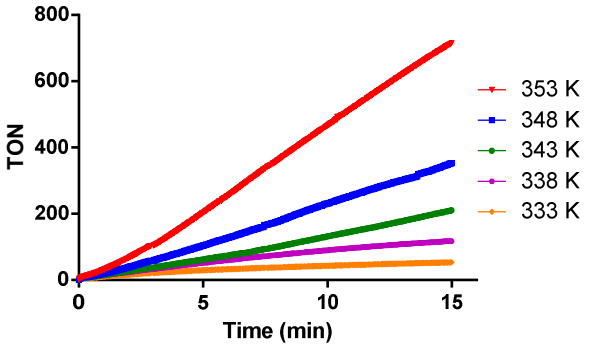

Fig. 5 Representation of TON (mol of H_2 per mol of Rh) *vs.* time of the solventless FA dehydrogenation catalysed by **1** (0.016 % mol) in the presence of HCOONa (30 % mol) at different temperatures.

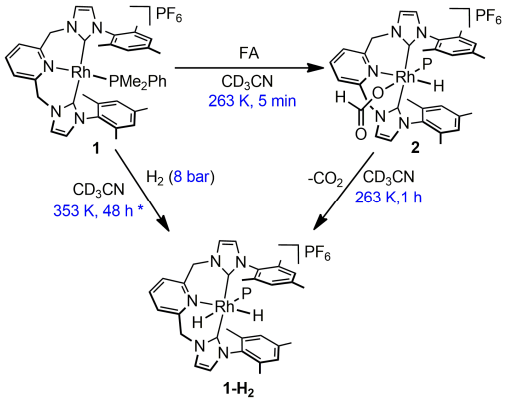

Scheme 2. Reactivity of complex **1** with FA and H_2, giving rise to species **2** and **1-H_2** (P = PMe_2Ph). *This reaction never went to completion, even under harsher conditions.

Interestingly, we observed that there is a strong dependence of the catalyst´s activity and durability with temperature. Even though catalyst activity and TON values remain low at 333K, when the temperature reaches 343 K the life of the catalyst increases considerably, reaching a TON value of 3400, which is a greater value than that achieved at 353 K; however, under these conditions catalyst **1** presents a modest activity on FA dehydrogenation associated with a TOF value of 3559 h^{-1}. When temperature reaches 363 K, TON values are quite similar than those observed at 353 K (TOF = 4984 h^{-1}); such catalytic activity, in spite of be greater than that obtained at 353 K, Eyring plot shows a loss of the lineal progression of the FA dehydrogenation activity with the temperature (see Fig. S26), which indicates that high temperatures may compromise the stability of **1** in the catalytic media. This statement becomes evident at 373 K, where TON and TOF values fall, which indicates that despite the fact that temperature is a key parameter to improving the catalyst´s activity and catalyst´s life, high temperatures values boost catalyst decomposition.

NMR Studies

In order to gain more insight into the operative mechanism of FA dehydrogenation performed by cationic complex **1**, we carried out a series of NMR experiments in combination with DFT theoretical studies. Firstly, we monitored the direct interaction of **1** with variable amounts of FA in CD_3CN by NMR techniques; in this way, addition of neat FA to a solution of **1** in CD_3CN in a 1:1 ratio at RT resulted in a quick reaction that allowed observing for a short time a monohydrido species, along with unreacted **1**. Furthermore, a typical signal of molecular hydrogen is observed at $\delta(^1H)$ 4.56 ppm along with two weak signals in the hydride area at $\delta(^1H)$ –9.43 and –17.18 ppm. Then, a variable temperature NMR study was carried out. When **1** was treated with FA in a 1:3 molar ratio in CD_3CN at low temperatures (268-282 K) in a sealed J Young NMR tube, the initial deep red colour changed to yellow (which agrees with the colour change observed under catalytic conditions), and the ^1H NMR spectrum of the mixture showed, upon 5 min of standing, a clean transformation to monohydrido species, further characterized as formate hydrido Rh^{III} complex $[(CNC)^{Mes}Rh(\kappa^O\text{-}OC(O)H)(PMe_2Ph)H]PF_6$ (**2**; Scheme 2). Interestingly, when **1** was reacted with FA in a 1:3 molar ratio at room temperature, only bis(hydrido) species **1-H_2** and starting complex **1** were detected in the NMR spectra, while no monohydrido **2** was observed in the mixture (Figures S11-S12). All these results suggest that there is an dynamic equilibrium in solution between **1**, **2** and **1-H_2** throughout the FA deshydrogenation process.

Interestingly, we were able to isolate formate complex **2** as a yellow solid by reacting complex 1 with 3 molar-equiv. of neat FA at 253 K in acetonitrile (see Experimental Section). Intermediate formate complex **2** has been characterized through a combination of NMR techniques (Figures S13-S19). The ^1H NMR spectrum of 2 in CD_3CN showed a pseudo triplet at $\delta(^1H)$ –15.62 ppm (J = 21.2 Hz), signalling the presence of a hydrido ligand bound to the metal, *cis* to the phosphane ligand ($\delta(^{31}P)$ 37.0 ppm, $^1J_{P-Rh}$ = 135 Hz). The presence of the formate ligand in **2** was evident from the resonance observed at $\delta(^1H)$ 8.32 ppm, assigned to the formate proton, which correlated to a singlet observed at $\delta(^{13}C)$ 166.2 ppm in the $^{13}C\{^1H\}$-APT NMR spectrum corresponding to the carboxylic C atom. The ligand skeleton in 2 reflected an averaged C_{2h} symmetry in solution, due to the observation of a sole signal (dd) for the carbenic atoms in the $^{13}C\{^1H\}$-APT NMR spectrum of **2** ($\delta(^{13}C)$ 171.9 ppm, $^1J_{C-Rh}$ = 35 Hz, $^2J_{C-P}$ = 14 Hz). Also, the =CH protons of both imidazolium moieties were observed as two separated doublets in the ^1H NMR spectrum of **2**, which correlated with signals at $\delta(^{13}C)$ 125.9 and 125.8 ppm in the $^{13}C\{^1H\}$-APT NMR spectrum, respectively.

The stereochemistry of compound **2** was well established by ^1H-^1H NMR NOESY experiments; more specifically, we observed a strong NOE effect between the hydrido ligand and the *meta* protons of the phenyl group of the phosphane ligand, and also with one methyl moiety from the mesityl group, which located the hydrido ligand *trans* to the pyridinic N atom (Fig. 6). Species **2** is well depicted in Scheme 2; the hydrido and formate ligands are mutually *cis* as a consequence of an oxidative addition of the O–H bond of a FA molecule to the Rh^I centre, in agreement with DFT calculations (see below). Once the nature of complex **2** was well established, we continued monitoring the reaction of 1 with 3 molar-equiv. of FA by NMR techniques in CD_3CN by gradually increasing the temperature.

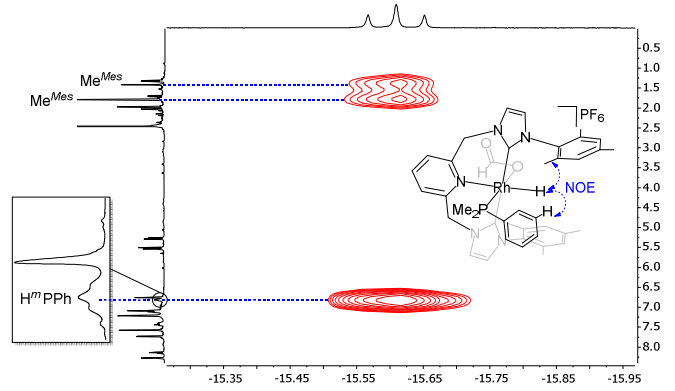

Fig. 6 Selected region of the ^{1}H-^{1}H NOESY NMR spectrum of [(CNC)^{Mes}Rh(κ^{O}-OC(O)H)(PMe$_2$Ph)H]PF$_6$ (**2**) in CD$_3$CN at 263 K.

Upon formation of **2** after 5 min at 268 K, the temperature was increased to 278 K; after 10 min, two incipient signals of hydrido ligands were detected, which became more intense after 30 min of standing at 282 K. Upon 1h the ^{1}H NMR spectrum of the reaction showed the presence of two different species, hydrido formate **2** and a new bis(hydrido) complex, further characterized as [(CNC)^{Mes}Rh(PMePh$_2$)H$_2$]PF$_6$ (**1-H$_2$**, Scheme 2). Fig. 7 shows the hydride area of the ^{1}H NMR spectra of the reaction between **1** and FA in CD$_3$CN at variable temperature. Complex **1-H$_2$** is characterized by two hydrido resonances: a doublet of doublets at $\delta(^{1}H)$ –9.43 ppm ($^{2}J_{H-P}$ = 173.4 Hz; $^{1}J_{H-Rh}$ = 24.8 Hz) and another doublet of doublets at $\delta(^{1}H)$ –17.18 ppm ($^{3}J_{H-P}$ = 17.4 Hz; $^{1}J_{H-Rh}$ = 28.9 Hz), while the $^{31}P\{^{1}H\}$ NMR spectrum showed a broad doublet at $\delta(^{31}P)$ –8.4 ppm ($^{1}J_{P-Rh}$ = 153 Hz). The location and integration of the hydrido signals clearly indicates a complex with two hydrido ligands in mutual *cis* disposition. Another diagnostic resonance of the bis(hydrido) complex **1-H$_2$** was the observation of an AB system centred at 5.03 ppm due to the CH$_2$ arms of the CNC^{Mes} ligand.

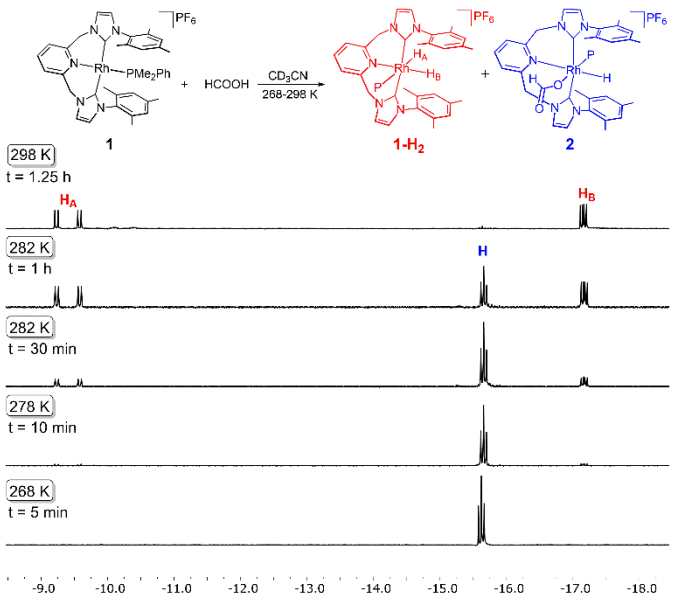

Fig. 7 Selected hydride region of the ^{1}H NMR spectra of the evolution of the reaction of **1** with 3 molar-equiv. of FA in CD$_3$CN at variable temperatures (268-298 K).

Given the nature and composition of the bis(hydrido) complex **1-H$_2$**, we tried its synthesis through direct hydrogenation of complex **2**. For that purpose, a J Young NMR tube was charged with **1**, dissolved in CD$_3$CN and pressurized with H$_2$ (8 bar). The NMR tube was sealed and heated at 353 K for 45 min. At this point, the ^{1}H NMR of the mixture showed incipient hydride signals. Upon heating overnight at 353 K, the initial red solution of **1** eventually transformed to a yellowish mixture containing the bis(hydrido) complex, tentatively characterized as [(CNC)^{Mes}Rh(PMePh$_2$)H$_2$]PF$_6$ (**1-H$_2$**, Scheme 2), along with some unreacted **1** (Fig. S20). From this experiment it is clear that access to **1-H$_2$** by oxidative addition of H$_2$ to **2** is a difficult process when compared to its formation *via* hydride abstraction of the hydrido formate complex **2**. The difficulty to achieve net addition of dihydrogen to **1** contrasts with the behaviour observed for the related deprotonated amido complex [(CNC)^{Mes}*Rh(PMe$_2$Ph)], which easily adds dihydrogen to afford the corresponding bis(hydrido) Rh^{III} complex [(CNC)^{Mes}*Rh(PMe$_2$Ph)H$_2$].[10]

Deuterium Labelling and KIE Experiments

In order to get a deeper insight in the **2**-catalysed FA dehydrogenation process, we performed some deuterium labelling experiments. We monitored the reaction of **1** with HCOOD in CDCN$_3$ at 253 K by ^{2}H NMR techniques, observing the formation of a broad resonance in the ^{2}H NMR spectrum at $\delta(^{2}H)$ –16.0 ppm. This signal corresponded to the Rh–D bond formed by oxidative addition of HCOO–D to 1, affording an isotopomer of **2**, namely [(CNC)^{Mes}Rh(κ^{O}-OC(O)H)(PMe$_2$Ph)D]PF$_6$ (2-D; Fig. S21-S22). Additionally, the ^{1}H NMR spectrum of the *in situ* reaction of fully deuterated FA (DCOOD) with 1 allowed us to observe, together with a signal of dihydrogen ($\delta(^{1}H)$ 4.56 ppm), a pattern of H–D coupling due to released gaseous HD (Fig. S23), which indicates that throughout the catalysis there is an exchange with the sodium formate of the medium. When the same experiment is carried out without sodium formate in the catalytic mixture, the formation of HD is not observed (absence of the H–D pattern in the ^{1}H NMR spectrum). These observations agreed to the KIE effect estimated where the use of DCOONa affects the reaction rate (K_{HCOONa}/K_{DCOONa}) = 1.51, Table 3, see below).

In order to gain insight into the rate-limiting step of the FA dehydrogenation by complex **1**, we performed H/D kinetic isotopic effect (KIE) experiments with **1** as catalyst (Table 3). The KIE obtained upon changing HCOOH to DCOOD (2.58) and that from HCOOH to DCOOH (2.44) firmly suggests that the rate-limiting step in the proposed mechanism involves the C–H bond cleavage of a formate ligand, a process that may occur through β-hydride elimination or hydride abstraction. Interestingly, the experiment with deuterated sodium formate (DCOONa) has a slope that falls right in the middle of both groups, which supports the postulation of the C–H bond cleavage being the rate-limiting step. Furthermore, the H/D kinetic isotopic effects measured for HCOOH/HCOOD and DCOOD/DCOOH experiments (1.05 and 1.17, respectively) suggest that O–H cleavage is not involved in the turnover limiting step.

Table 3 Kinetic isotope effect data.

FA derivative	K	K_{rel}	KIE effect (observed)
HCOOH	240.14	1	k_{DCOOD}/k_{DCOOH} = 1.05
DCOOD	92.79	2.58	k_{DCOOD}/k_{HCOOD} = 2.21
DCOOH	98.06	2.44	k_{HCOOH}/k_{HCOOD} = 1.17
HCOOD	204.78	1.17	k_{HCOOH}/k_{DCOOD} = 2.58
30 % DCOONa/HCOOH	158.19	1.51	k_{HCOOH}/k_{DCOOH} = 2.44
			k_{HCOONa}/k_{DCOONa} = 1.51

DFT Studies on Catalytic FA Dehydrogenation by 1

DFT studies were performed in order to gain better insight into the operative mechanism of FA dehydrogenation catalysed by complex **1**. Two alternative pathways have been considered, the first of them starting by the activation of the formate and the second one from the activation of the formic acid. The former path would start by the hydride abstraction step from the formate by the metal complex. However, the calculated activation energy for this step is energetically unaffordable (TSBC' 27.4 kcal mol^{-1}, see Fig. S27) while the second pathway yields lower energetic barriers. The relative Gibbs energy profile calculated using DFT methodology is provided in Fig. 8. As the reaction takes place in FA media, microsolvation of strong hydrogen donors and acceptors is considered in the proposed species throughout the catalytic cycle.

The initial step in FA dehydrogenation involves the *O*-coordination of a FA molecule to **1**. This coordination to the metal induces decoordination of the pyridinic N atom generating intermediate **B**, in which the Rh^{I} maintains a square planar geometry. This is an endergonic process where the energy increases to 9.1 kcal mol^{-1} and induces a conformational change within the bulky $(CNC)^{Mes}$* and PMe_2Ph ligands. Following that, intramolecular O–H oxidative addition of coordinated FA proceeds through **TSBC** (9.4 kcal mol^{-1}), affording Rh^{III} hydrido formate intermediate **C**, in which the hydrido ligand is located *trans* to the pyridinic N atom. Intermediate C presents a relative energy of –12.1 kcal mol^{-1} and its stereochemistry agrees with the NMR data obtained for intermediate **2**. Subsequent addition of a second FA molecule leads to adduct **C** + FA stabilized by hydrogen bonding with the formate ligand. At this point, protonation of the hydride intermediate **C** by formic acid, yields a Rh^{III} bis(formate) intermediate, **F**, and molecular H_2, which could be a viable pathway to close the catalytic cycle. However, the calculated relative energy of **F** amounts to 14.7 kcal mol^{-1} (see Fig. S28), being energetically unaffordable. Instead, the κ-*O*-formate ligand switches its coordination mode from κ-*O* to κ-*H* via transition state **TSCD**, with a relative energy of 1.7 kcal mol^{-1}. Then, hydrogen abstraction from the formate anion to the metal is characterized by **TSDE**, showing an overall energy barrier of 16.9 kcal mol^{-1} (from intermediate **C**) leading to the dihydride intermediate **E** and releasing a CO_2 molecule (–5.2 kcal mol^{-1}). Finally, a H_2 molecule can be formed by heterolytic bond formation between the negatively charged hydride and the positively charged proton of a FA molecule. This process is characterized by **TSEC** with a relative energy of 0.2 kcal mol^{-1}. The release of H_2 is exergonic (–17.3 kcal mol^{-1}) and leads to the intermediate **C** + **FA**, closing the catalytic cycle.

Based on this DFT study, complex **1** is activated by oxidative addition of the O–H bond of FA to the metal. Then, the catalytic cycle comprises three steps: i) change in the coordination mode of the formate ligand, ii) hydrogen abstraction to yield the dihydride and release of CO_2 and iii) H_2 formation between hydride and a proton from an external FA molecule. The rate determining step for the DFT calculated mechanism is the hydride abstraction step presenting an overall energetic barrier of 16.9 kcal mol^{-1} in good agreement with the obtained experimental data of 18.12 ± 1.17 kcal mol^{-1}. It should be noted that for other FA dehydrogenation catalysts the formation of the hydride intermediates takes place by β-elimination process, which results to the be the rate determining step[19]. In the present case, the lack of vacant sites at the metal impedes such mechanism similarly to other catalysts reported in the literature.[20]

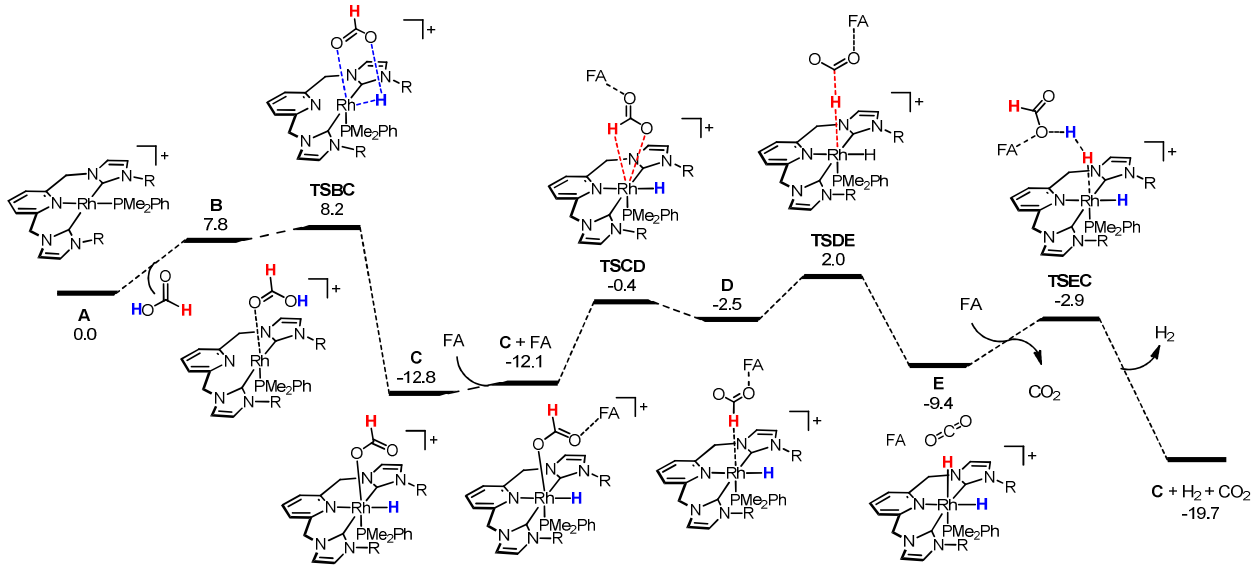

Fig. 8 DFT energetic profile (ΔG in kcal mol^{-1}, relative to **A** and isolated molecules) for formic acid dehydrogenation catalysed by **1**.

The KIEs have been calculated using DFT methodology for a direct comparison to experimental KIEs. According to the calculated energetic profile, the rate determinant structures are C and TSCE, the calculated KIE for DCOOH is 2.63, while for HCOOD is 1. This is in good agreement with the experimental values of 2.44 and 1.17 obtained in the previous section.

Conclusions

In summary, we have shown that Rh complex **1** behaves as an excellent catalyst for the dehydrogenation of FA under solvent-free conditions. The TOF values obtained for **1** are amongst the highest so far reported in the absence of solvent, which contrasts with the modest catalytic activities reported for Rh-complexes in the dehydrogenation of FA. The astounding performance of **1** could be attributed to the bis-NHC scaffold of the pincer ligand and also to the presence of the P-donor PMe_2Ph ligand. NHC ligands give rise to electron-rich metal centres and strong C–metal bonds; therefore, the presence of the $(CNC)^{Mes}$ pincer ligand chosen by us for this study plausibly eases the formation of the active species **2** and stabilises the Rh^{III} intermediates of the catalytic cycle. The DFT calculations support a catalytic cycle that involves a hydride abstraction step, which converts monohydride **C** into bis(hydrido) **E**; followed by protonation of the bis(hydrido) **E** to regenerate **C**. The formation of the active species, **C** (**2**), takes place via oxidative addition of FA to **A** (**1**). The calculated reaction mechanism agrees well with experimental data: (i) Key intermediates of the catalytic cycle, **C** (**2**) and **E** (**1-H_2**), were observed and characterised *in situ* by NMR by means of stoichiometric reactions; (ii) KIE measurements suggest that the hydride abstraction is the rate-limiting step; (iii) the activation energies calculated by the Eyring model compare well with the theoretical value obtained from DFT calculations; (iv) labelling experiments confirm that the active species is formed by oxidative addition of the O–H bond of FA to the Rh(I) center in **1**.

Experimental

Procedure for FA dehydrogenation. FA dehydrogenation catalytic experiments were carried out as follows. The catalyst **1** (0.016 % mol) and sodium formate were weighted on an analytic balance placed into a drybox, and then transferred to a microreactor (*Man on the moon* series X102 kit), which was pre-heated at 353 K. Then, under an argon atmosphere, 2 mL of neat formic acid was injected into the reactor *via* syringe and left under stirring until complete dehydrogenation of FA. Pressure measurements were monitored by a manometer connected to the reactor.

Computational details. All DFT calculations were carried out using the Gaussian program package.[21] Geometrical optimizations and analytical frequency calculations were performed at the B3LYP-D3 method[22] including solvent corrections using the PCM method[23] for formic acid and the def2-SVP basis set,[24] together with the corresponding core potential for Rh atom. Energies were refined by single point calculations using the M06L functional[25] combined to SMD solvation model[26] and the def2-TZVP basis set. The "ultrafine" grid was employed in all calculations. All reported energies are Gibbs free energies referred to a 1 M standard state at 353 K and quasi harmonic corrections[27] calculated using the Goodvibes program.[27]

The nature of the stationary points was confirmed by analytical frequency analysis, and transition states were characterized by a single imaginary frequency corresponding to the expected motion of the atoms. Calculations of KIE from DFT data are obtained by replacing the mass of the selected hydrogen atom by deuterium using the keyword readisotopes in G09 and calculating the vibrational frequencies at the transition state and the corresponding intermediate.

Preparation of $[(CNC)^{Mes}Rh(\kappa^{O}\text{-}OC(O)H)(PMe_2Ph)H]PF_6$ (2).

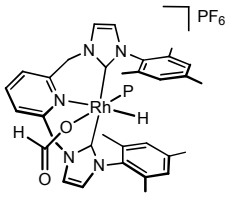

A Schlenk tube was charged with **1** (120 mg, 0.148 mmol) and dissolved in CH_3CN (5 mL). Then, 2 mol–equiv. of neat FA (11.2 µL, 0.202 mmol) was added *via* microsyringe and the resulting yellow solution was stirred for 10 min at 253 K. Evaporation of the volatiles by reduced pressure left a yellow residue, which was washed with hexanes and then vacuum-dried. Yield: 115 mg (86 %).

^{1}H RMN (400 MHz, CD_3CN, 253 K): δ 8.32 (s, 1H; HC(O)O–Rh), 8.13 (t, $^3J_{H-H}$ = 7.9 Hz, 1H; H^p py), 7.73 (d, $^3J_{H-H}$ = 7.7 Hz, 1H; H^m py), 7.56 (d, $^3J_{H-H}$ = 1.9 Hz, 2H; =CH Im), 7.48 (m, 2H; H^o Ph), 7.20 (d, $^3J_{H-H}$ = 1.9 Hz, 2H; =CH Im), 7.10 (m, 2H; H^m Ph), 7.08 (br s, 2H; CH Mes), 6.80 (m, 1H; H^m Ph), 6.74 (br s, 2H; CH Mes), 5.51 (d, $^3J_{H-H}$ = 16.5 Hz, 2H), 5.26 (d, $^3J_{H-H}$ = 16.5 Hz, 2H) (CH_2N), 2.55 (s, 6H), 1.78 (s, 6H), 1.41 (s, 6H) (Me Mes), 1.32 (d, $^2J_{H-P}$ = 10.4 Hz, 6H; CH_3P), –15.62 (t, $^1J_{H-Rh}$ = 21.2 Hz, $^2J_{H-P}$ = 21.2 Hz, 1H; Rh–H). ^{31}P {^{1}H} NMR (162 MHz, CD_3CN, 253 K): δ 27.0 (d, $^2J_{P-Rh}$ = 135 Hz). ^{13}C {^{1}H}-APT NMR (100 MHz, CD_3CN, 253 K): δ 171.9 (dd, $^1J_{C-Rh}$ = 35 Hz, $^2J_{C-P}$ = 14 Hz; Rh–C Im), 166.2 (s; HCOO–Rh), 156.8 (s; C^o py), 142.7 (C^p py), 136.9, 136.7, 135.8 (C_q Mes), 132.1, 131.9 (P*Ph*), 131.0, 130.4 (CH Mes), 129.9, 129.8 (P*Ph*), 127.7 (C^m py), 125.9, 125.8 (=CH Im), 55.7 (CH_2N), 21.5 (Me Mes), 171.9 (d, $^1J_{C-P}$ = 36 Hz; PMe), 19.1, 19.0 (Me Mes). Mass Calcd for $C_{40}H_{46}N_5O_2PRh$: 762.7048; HRMS (ESI^+): *m/z* 716.2408 (100%; M^+ – HCOOH).

Conflicts of interest

There are no conflicts to declare.

Acknowledgements

The authors express their appreciation for the financial support from projects PGC2018-099383-B-I00 (MCIU/AEI/FEDER, UE), RTI2018-099136-A-I00 (MCIU/AEI/FEDER, UE), DGA/FSE (group E42_20R) and CSIC project 202080I024. The co-author V.P. thankfully acknowledges the resources from the supercomputers "Memento" and the technical expertise and assistance provided by the Institute for Biocomputation and Physics of Complex Systems (BIFI)–Universidad de Zaragoza. A.

U. thankfully acknowledges the Spanish MECD for a FPU fellowship (FPU 2017/05417).

Notes and references

1 N. P. Brandon and Z. Kurban, Clean energy and the hydrogen economy. *Phil. Trans. R. Soc.*, 2017, **A375**: 20160400.

2 a) S. Enthaler, Carbon Dioxide—The hydrogen-storage material of the future?, *ChemSusChem*, 2008, **1**, 801–804. b) J. Eppinger and K. –W. Huang, Formic acid as a hydrogen energy carrier, *ACS Energy Lett.*, 2017, **2**, 188–195. c) F. Joó, Breakthroughs in hydrogen storage—formic acid as a sustainable storage material for hydrogen *ChemSusChem*, 2008, **1**, 805–808.

3 a) S. Thomas, CO_2-based hydrogen storage: CO_2 hydrogenation to formic acid, formaldehyde and methanol, *Phys. Sci. Rev.*, 2018, 20170015. b) U. Praveenkumar and S. Vivek, Carbon sequestration: hydrogenation of CO_2 to Formic acid, *Present Environ. Sustain. Dev.*, 2016, **10**, 13–34.

4 a) F. Valentini, V. Kozell, C. Petrucci, A. Marrocchi, Y. Gu, D. Gelman and L. Vaccaro, Formic acid, a biomass-derived source of energy and hydrogen for biomass upgrading, *Energy Environ. Sci.*, 2019, **12**, 2646–2664. b) D. A. Bulushev and J. R. H. Ross, Towards sustainable production of formic acid, *ChemSusChem,* 2018, **11**, 821–836.

5 D. J. Drury in *FA and Derivatives*. *Kirk-Othmer Encyclopedia of Chemical Technology,* Vol. 27 (Eds.: J. I. Kroschwitz and M. Howe-Grant), John Wiley & Sons, Inc.: New York, 2013.

6 a) K. Sordakis, C. Tang, L.K. Vogt, H. Junge, P.J. Dyson, M. Beller and G. Laurenczy, Homogeneous catalysis for sustainable hydrogen storage in formic acid and alcohols, *Chem. Rev.*, 2018, **118**, 372–433. b) P. Stathi, M. Solakidou, M. Louloudi and Y. Deligiannakis, From homogeneous to heterogenized molecular catalysts for H_2 production by formic acid dehydrogenation: mechanistic aspects, role of additives, and co-Catalysts, *Energies*, 2020, **13**, 733. c) M. Grasemann and G. Laurenczy, Formic acid as a hydrogen source—recent developments and future trends, *Energy Environ. Sci.*, 2012, **5**, 8171–8181. d) A. Luque-Gómez, S. García-Abellán, J. Munarriz, V. Polo, V. Passarelli and M. Iglesias, Impact of green cosolvents on the catalytic dehydrogenation of formic acid: the case of iridium catalysts bearing NHC-phosphane ligands, *Inorg. Chem.*, 2021, **60**, 15497−15508.

7 a) J. J. A. Celaje, Z. Lu, E. A. Kedzie, N. J. Terrile, J. N. Lo and T. J. Williams, A prolific catalyst for dehydrogenation of neat formic acid, *Nat. Commun.*, 2016, **7**, 11308. b) A. Iturmendi, M. Iglesias, J. Munarriz, V. Polo, V. Passarelli, J. J. Pérez-Torrente and L. A. Oro, A highly efficient Ir-catalyst for the solventless dehydrogenation of formic acid: the key role of an N-heterocyclic olefin, *Green Chem.*, 2018, **20**, 4875–4879. c) S. Cohen, V. Borin, I. Schapiro, S. Musa, S. De-Botton, N. V. Belkova and D. Gelman, Ir(III)-PC(sp^3)P bifunctional catalysts for production of H_2 by dehydrogenation of formic acid: experimental and theoretical study, *ACS Catal.*, 2017, **7**, 8139–8146. d) S. Wang, H. Huang, T. Roisnel, C. Bruneau and C. Fischmeister, Base-free dehydrogenation of aqueous and neat formic acid with iridium(III) Cp*(dipyridylamine) catalysts, *ChemSusChem*, 2019, **12**, 179–184.

8 S. Kar, M. Rauch, G. Leitus, Y. Ben-Davis and D. Milstein, Highly efficient additive-free dehydrogenation of neat formic acid, *Nat. Catal.*, 2021, **4**, 193–201.

9 a) M. Albrecht, *Chem. Rev.*, 2010, **110**, 576–623. b) K. R. Jain, W. A. Herrmann and F. E. Kühn, High oxidation state transition metal complexes ligated with N-heterocyclic carbenes, *Curr. Org. Chem.*, 2008, **12**, 1468–1478. c) M. Iglesias and L. A. Oro, A leap forward in iridium–NHC catalysis: new horizons and mechanistic insights, *Chem. Soc. Rev.*, 2018, **47**, 2772–2808.

10 P. Hermosilla, P. García-Orduña, F. J. Lahoz, V. Polo and M. A. Casado, Rh complexes with pincer carbene CNC lutidine-based ligands: reactivity studies toward H_2 addition, *Organometallics*, 2021, **40**, 3720−3732.

11 a) J. B. Curley, N. E. Smith, W. H. Bernskoetter, N. Hazari and B. Q. Mercado, Catalytic formic acid dehydrogenation and CO_2 hydrogenation using iron PN^RP pincer complexes with isonitrile ligands, *Organometallics*, 2018, **37**, 3846−3853. b) S. Oldenhof, J. I. van der Vlugt and J. N. H. Reek, Hydrogenation of CO_2 to formic acid with iridium^{III} (bisMETAMORPhos) (hydride): the role of a dormant *fac*-Ir^{III} (trihydride) and an active *trans*-Ir^{III} (dihydride) species, *Catal. Sci. Technol.*, 2016, **6**, 404–408.

12 P. Rodziewicz and N. L. Doltsinis, Formamide dimers: a computational and matrix isolation study, *J. Phys. Chem. A*, 2009, **113**, 6266–6274.

13 S. Fukuzumi, T. Kobayashi and T. Suenobu, Unusually large tunneling effect on highly efficient generation of hydrogen and hydrogen isotopes in pH-selective decomposition of formic acid catalyzed by a heterodinuclear iridium−ruthenium complex in water, *J. Am. Chem. Soc.*, 2010, **132**, 1496–1497.

14 a) S. Siek, D. B. Burks, D. L. Gerlach, G. Liang, J. M. Tesh, C. R. Thompson, F. Qu, J. E. Shankwitz, R. M. Vasquez, N. Chambers, G. J. Szulczewski, D. B. C. Grotjahn, E. Webster and E. T. Papish, Iridium and ruthenium complexes of N-heterocyclic carbene- and pyridinol-derived chelates as catalysts for aqueous carbon dioxide hydrogenation and formic acid dehydrogenation: the role of the alkali metal, *Organometallics*, 2017, **36**, 1091–1106. b) J. F. Hull, Y. Himeda, W. –H. Wang, B. Hashiguchi, R.; Periana, D. J. Szalda, J. T. Muckerman and E. Fujita, Reversible hydrogen storage using CO_2 and a proton-switchable iridium catalyst in aqueous media under mild temperatures and pressures, *Nat. Chem*., 2012, **4**, 383–388. c) S. Fukuzumi, T. Kobayashi and T. Suenobu, Efficient catalytic decomposition of formic acid for the selective generation of H_2 and H/D exchange with a water-soluble rhodium complex in aqueous solution, *ChemSusChem*, 2008, **1**, 827–834. d) Y. Himeda, Highly efficient hydrogen evolution by decomposition of formic acid using an iridium catalyst with 4,4′-dihydroxy-2,2′-bipyridine, *Green Chem.*, 2009, **11**, 2018–2022. e) W. –H. Wang, M. Z. Ertem, S. Xu, N. Onishi, Y. Manaka, Y. Suna, H. Kambayashi, J. T. Muckerman, E. Fujita and Y. Himeda, Highly robust hydrogen generation by bioinspired Ir complexes for dehydrogenation of formic acid in water: experimental and theoretical mechanistic investigations at different pH, *ACS Catal*., 2015, **5**, 5496–5504.

15 S. Patra, M. K. Awasthi, R. K. Rai, H. Deka, S. M. Mobin and S. K. Singh, Dehydrogenation of formic acid catalyzed by Water-soluble ruthenium complexes: X-ray crystal structure of a diruthenium complex, *Eur. J. Inorg. Chem*., 2019, 1046–1053.

16 X. –T. Guo, J. Zhang, J. –C. Chi, Z. –H. Li, Y. –C. Liu, X. –R. Liu and S. –Y. Zhang, Efficient dehydrogenation of a formic Acid–ammonium formate mixture over Au_3Pd_1 catalyst, *RSC Adv*., 2019, **9**, 5995–6002.

17 C Fink and G. Laurenczy, A precious catalyst: rhodium-catalyzed formic acid dehydrogenation in water, *Eur. J. Inorg. Chem.,* 2019, 2381–2387.

18 N. J. Britto and M. Jaccob, Deciphering the mechanistic details of manganese-catalyzed formic acid

dehydrogenation: insights from DFT calculations, *Inorg. Chem.*, 2021, **60**, 11038−11047.
19 M. Iglesias and L. A. Oro, Mechanistic considerations on homogeneously catalyzed formic acid dehydrogenation, *Eur. J. Inorg. Chem.*, 2018, 2125−2138.
20 a) T. Zell, B. Butschke, Y. Ben-David and D. Milstein, Efficient hydrogen liberation from formic acid catalyzed by a well-defined iron pincer complex under mild conditions, *Chem. Eur. J.*, 2013, **19**, 8068−8072. b) I. Mellone, N. Gorgas, F. Bertini, M. Peruzzini, K. Kirchner and L. Gonsalvi, Selective formic acid dehydrogenation catalyzed by Fe-PNP pincer complexes based on the 2,6-diaminopyridine scaffold, *Organometallics*, 2016, **35**, 3344−3349. c) E. A. Bielinski, P. O. Lagaditis, Y. Zhang, B. Q. Mercado, C. Würtele, Bernskoetter, W. H. N. Hazari and S. Schneider. Lewis acid-assisted formic acid dehydrogenation using a pincer-supported iron catalyst, *J. Am. Chem. Soc.*, 2014, **136**, 10234−10237. d) S. Oldenhof, M. Lutz, B. de Bruin, J. I. van der Vlugt and J. N. H. Reek, Dehydrogenation of formic acid by Ir–bisMETAMORPhos complexes: experimental and computational insight into the role of a cooperative ligand, *Chem. Sci.*, 2015, **6**, 1027-1034.
21 Gaussian 09, revision D.01; Gaussian, Inc.; Wallingford CT, 2016. See SI for full citation
22 a) A. D. Becke, A new mixing of Hartree–Fock and local density-functional theories, *J. Chem. Phys.*, 1993, **98**, 1372–1377. b) C. Lee, W. Yang and R. G. Parr, Development of the Colle-Salvetti correlation-energy formula into a functional of the electron density, *Phys. Rev. B*, 1988, **37**, 785–789. c) S. Grimme, J. Antony, S. Ehrlich and H. Krieg, A consistent and accurate ab initio parametrization of density functional dispersion correction (DFT-D) for the 94 elements H-Pu, *J. Chem. Phys.*, 2010, **132**, 154104. d) E. R. Johnson and A. D. Becke, A post-Hartree-Fock model of intermolecular interactions: inclusion of higher-order corrections, *J. Chem. Phys.*, 2006, **124**, 174104.
23 a) S. Miertuš, E. Scrocco and J. Tomasi, Electrostatic interaction of a solute with a continuum. A direct utilizaion of AB initio molecular potentials for the prevision of solvent effects, *Chem. Phys.,* 1981, **55**, 117–129; b) S. Miertuš, E. Scrocco and J. Tomasi, Approximate evaluations of the electrostatic free energy and internal energy changes in solution processes, *J. Chem. Phys.,* 1982, **65**, 239–245.
24 F. Weigend and R. Ahlrichs, Balanced basis sets of split valence, triple zeta valence and quadruple zeta valence quality for H to Rn: Design and assessment of accuracy, *Phys. Chem. Chem. Phys.,* 2005, **7**, 3297-305.
25 Y. Zhao and D. G. Truhlar, A new local density functional for main-group thermochemistry, transition metal bonding, thermochemical kinetics, and noncovalent interactions, *J. Chem. Phys.,* 2006, **125**, 194101.
26 A. V. Marenich, C. J. Cramer and D. G. Truhlar, Universal solvation model based on solute electron density and a continuum model of the solvent defined by the bulk dielectric constant and atomic surface tensions, *J. Phys. Chem. B*, 2009, **113**, 6378–6396.
27 S. Grimme, Supramolecular Binding Thermodynamics by Dispersion-Corrected Density Functional Theory, *Chem. Eur. J.*, 2012, **18**, 9955-9964.
28 G. Luchini, J. V. Alegre-Requena, I. Funes-Ardoiz and R. S. Paton, F1000Research, 2020, 9, 291. GoodVibes version 3.1.1 DOI: 10.12688/f1000research.22758.1.